Experimental Investigation of Large Area Transpired Solar Air Collectors

Lucio Mesquita[1], Gary Johnson[2], Ross Breton[2] and Stephen Harrison[2]

[1] Natural Resources Canada, CanmetENERGY-Ottawa, Ottawa (Canada)

[2] QSBR Innovations, Kingston (Canada)

Abstract

Single-pass transpired solar air systems are one of the most cost-effective solar thermal technologies available in the market due to their simplicity and robustness. While most experimental work in this area deals with small samples, the present work evaluates the performance of a large-area transpired solar air collector operating under natural atmospheric conditions. The collector array evaluated was unglazed and was equipped with a perforated metal absorber panel through which air was drawn and heated during operation. The absorber surface was coated with a spectrally-selective Low-e coating. Tests were performed between December 2023 and March 2024 at the Canadian National Solar Test Facility (NSTF) located in Mississauga, ON, Canada. During monitoring, the thermal performance of the installation was evaluated at two air flow rate conditions, typical of real installations. Although integrated into the building's wall, the system was not connected to the building ventilation system to allow for continuous operation for the study. This provided a level of operational independence that is usually not possible in field evaluations. The present work presents the results of the experiment with an analysis of the collector's efficiency as a function of ambient air temperature, wind speed and air flow rate.

Keywords: transpired collector, solar air heating, ventilation, perforated collector, solar thermal

1. Introduction

Transpired solar air systems are one of the most cost-effective solar thermal technologies available in the market due to their simplicity and robustness. Initially developed in the 1990's, several contributions in the literature have covered both theoretical and experimental investigations of the technology. Kutscher et al. (1991) developed an initial model with experimental validation through a small flat-plate sample. Brunger et al. (1999) evaluated several aspects of the technology, including description of demonstration projects, simulation and design tools and laboratory testing of small samples. Fleck et al (2002) measured the field performance of a large area transpired air collector, noting significant performance variation due to wind effects. However, the operational conditions related to suction air speed were not optimal during the experiments due to issues with one of the air blowers. Shukla et al (2012) reviewed the state-of-the-art of the technology.

While small samples have frequently been used for experimental study, they carry an inherent disadvantage. For example, the suction of air through the transpired surface causes a reduction of the boundary layer thickness, causing a reduction in convection losses. This effect, however, is difficult to capture when testing small samples. Small samples, however, do carry the advantage of being tested under controlled conditions with solar and wind simulators.

The motivation for the current work comes from a desire to better understand the performance of large scale transpired air solar collectors operating under real atmospheric conditions, and to study the relationship between small samples tested under steady-state conditions in simulated environments for rating purposes. The data captured during this investigation represents a significant source of information on the performance of these types of solar thermal collectors. This paper is an initial analysis of selected samples taken from the monitored data.

Selection and/or peer review under responsibility of Scientific Committee
10.18086/eurosun.2024.07.13 Available at http://proceedings.ises.org

2. Experimental Description

2.1 Test System

For this experiment, a large-area transpired air solar collector array was installed at the National Solar Test Facility (NSTF) located in Mississauga, Ontario, Canada. The installed collectors were equipped with a spectrally-selective low-emittance surface coating. The collectors followed the building wall orientation of 53° SE. Although integrated into the building wall, the system was not connected to the building ventilation system and was "single pass". This provided a level of operational independence that is usually not possible in field evaluations.

The focus of this study is the single collector array equipped with the spectrally selective absorber surface. The overall specifications of the selective absorber collector array studied in this paper are given in Table 1. A close-up photograph of the perforated absorber surface is shown in Fig. 1. The cross-section surface profile and dimensions of the absorber sheet are shown, Fig. 2. Figures 3 and 4 show the collector array during and after installation.

Tab. 1: Solar Collector Array Specifications

Collector Type	Single-stage, unglazed, transpired absorber, air solar collector
Collector coating	Low-e Selective surface
Gross dimensions	9.255 m W x 10.58 m H (97.9 m^2)
Plenum depth	0.205 m
Outlet Port Size	1.83 m W x 1.22 m H
Absorber	Aluminum sheet (0.75 mm)
Absorptance, α	0.935 (SRCC, 2020)
Emittance, ε	0.025 (SRCC, 2020)

Fig. 1: Closeup of perforated aluminum selective surface.

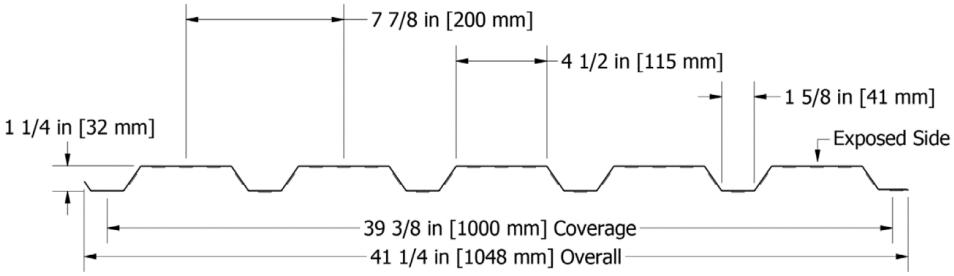

Fig. 2: Cross-section profile and dimensions of the absorber sheet.

Fig. 3: Transpired solar air collectors under construction at the Canadian National Solar Test Facility.

Fig. 4: Installed collectors. left: unglazed, selective surface model, right: two-stage black paint model.

2.2 Experimental configuration, Instrumentation and Data Acquisition

The assembled collector array was instrumented to monitor solar and infrared radiation incident on the collector's surface, horizontal direct and diffuse solar irradiance, barometric pressure, ambient air temperature and humidity, and wind speed and direction, Fig. 5.

During operation, outdoor ambient air was drawn through the solar collector's perforated absorber plate and directed through 20" diameter duct sections to the intake of a variable speed, centrifugal blower located in the building interior. The heated air exited the solar collector through an outlet manifold located in the upper periphery of the solar array. The outlet manifold directed the airflow through the building wall where the average outlet air temperature was measured by a 12-junction thermocouple array before it entered a flow nozzle to measure the volumetric flow rate. The pressure differential across the nozzle and duct air-temperature and pressure were recorded to calculate air mass flowrate. Thermocouples were installed on the back surface of the solar collector's absorber plate, and the exterior and interior surface of the wall behind the collector to estimate heat transmission through the wall.

Propeller/vane anemometers were installed on the rooftop and ahead of the panels to determine wind speed and direction. To measure total radiation (direct and diffuse) on the vertical wall, a PSP Pyranometer was mounted in the plane of the transpired panels, Fig. 6. A Precision infrared radiometer (PIR) was also mounted in the plane of the transpired panels. Global and Diffuse horizontal radiation were captured by an SPN1 Delta-T Pyranometer installed on a tower 15 m South of the panels. An ultrasonic anemometer was also placed at 2.5 meters directly in front of the panels to measure the U, V, and W components of wind velocity, Fig. 7. A temperature and humidity sensor was installed at ground level to measure local air properties at the site.

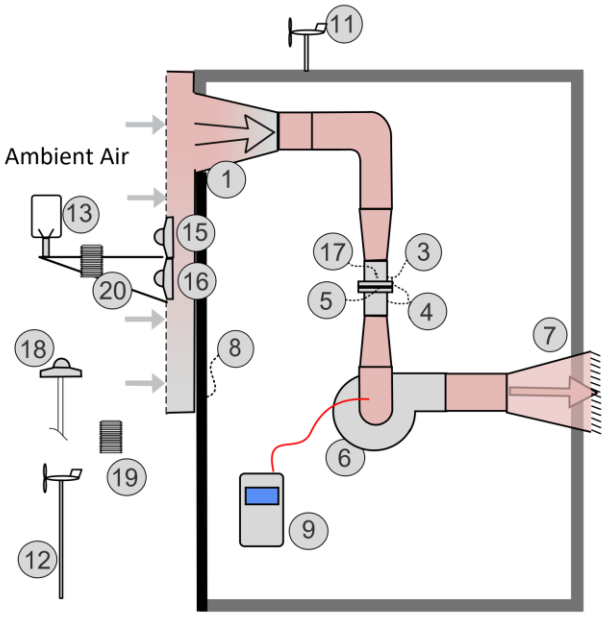

Fig. 5: Schematic of the experimental flow configuration, measurement points and instrumentation. Refer to Table 2 for the specifications of the numbered instrumentation.

All data was recorded by a PC running Windows 10® and LabVIEW 2020®. A "virtual instrument VI" was written specifically for the project. Values were stored at approximately 1-minute intervals during daylight hours and written as CSV (Excel) compatible data files for post analysis.

An Agilent data acquisition unit attached to the PC recorded raw sensor signals. An SPN1 Pyranometer transmitted both global and diffuse radiation as text values through an RS232 interface at polled intervals directly to LabVIEW.

The 3-axis ultrasonic anemometer components of the U, V, and W velocities were transmitted through an RS485 interface to the host computer/LabVIEW VI and captured at 4 Hz, then stored as daily numeric data files. The ultrasonic wind component values (U, V, W) were averaged over 1-minute intervals and stored.

Analysis and processing of the recorded data was performed using an MS Excel spreadsheet.

A photo of the interior of the building showing the wall directly behind the solar collector is shown in Figure 8. The ducting, hardware and measurement points are shown and numbered in the photo. Volumetric flowrates through the solar collector could be varied using a Variable Frequency Drive (VFD) to control blower motor frequency. Refer to Table 2 for the specifications of the indicated components.

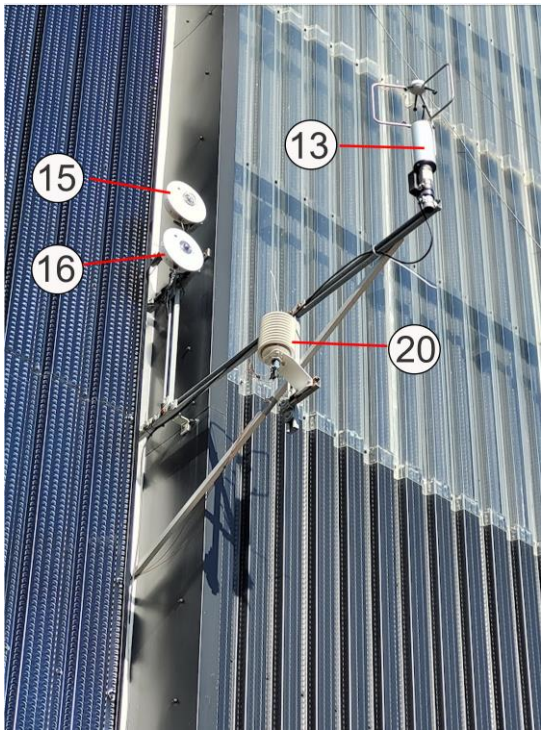

Fig. 6: Eppley PSP (15) and PIR (16) Pyranometers, ambient temperature sensors (20), and ultrasonic anemometer (13).

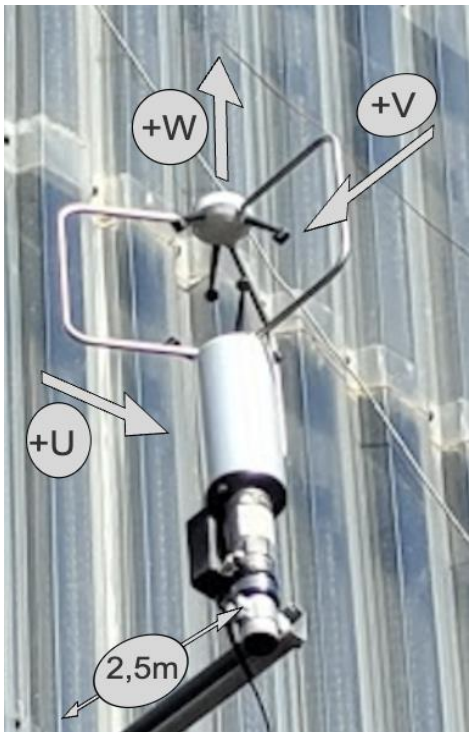

Fig. 7: 3-D Ultrasonic anemometer with direction of vectors U, V, and W relative to panel surface

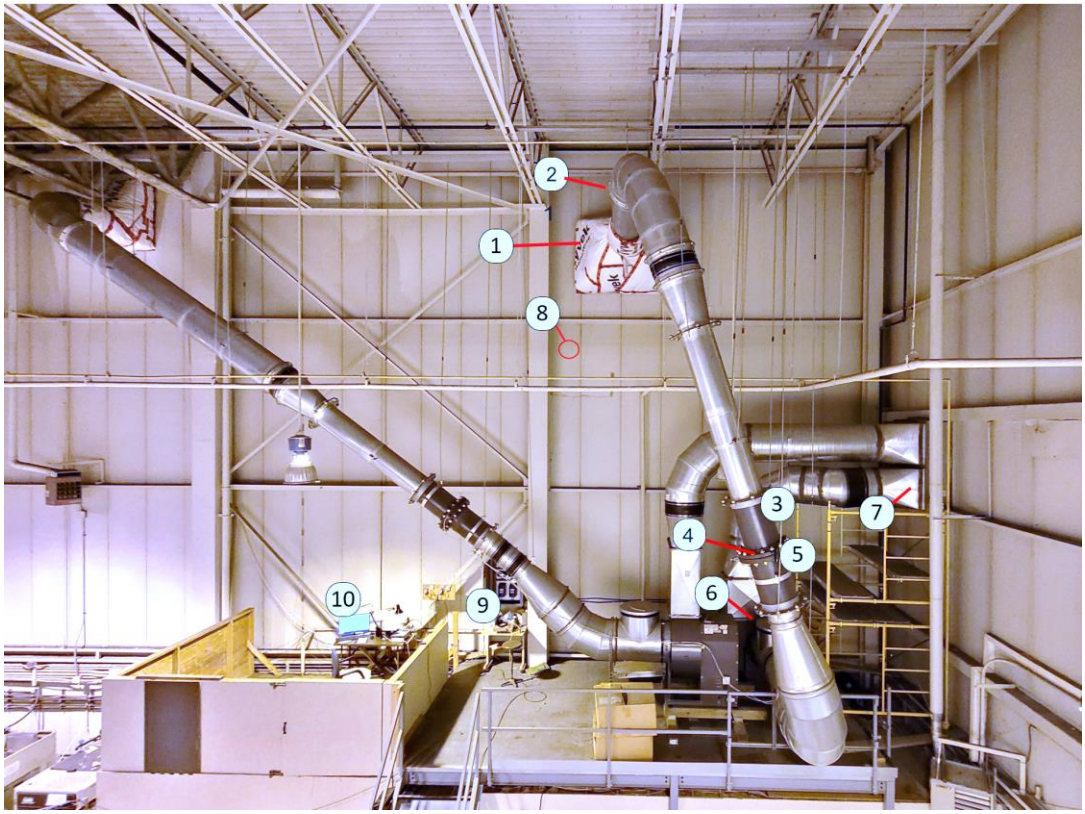

Fig. 8: Ducting for the system on the interior of the building showing the flow configuration and instrumentation. Outlet of the collector is at the top (1) . See Table 2 for the instrument specifications associated with the number tags.

Tab 2: Equipment and Instrumentation List

#	Instrument/equipment	Make/Model	Range	Accuracy*
1	Collector outlet manifold	NA	1.83 m x 1.22 m	-
2	Thermocouple array 2x6	Type T, thermocouple	-25 to 50˚C	±0.5 K
3	Static pressure selective	Vaisala PTB110	800 to 1100 hPa	±0.3 hPa
4	Δ pressure selective	Setra, model 264	0-250 Pa, 0-2.5 kPa	±1.0 % FS
5	Venturi	PIFS, MII# B14822	0.5 to 5 m^3 s^{-1}	±0.5 %
6	Blower	NA	-	-
7	Exhaust out of Bldg.	NA	NA	-
8	Wall temperatures	Type T, thermocouple	-25 to 50˚C	±0.5 K
9	Blower speed control	Lenze SMV	0 to 60 Hz	-
10	Data system	Agilent 34972a	-	-
11	Rooftop Wind monitor	Young, model 5103L	1 to 100 m s^{-1}, 360˚	±0.3 m s^{-1}, ±5°
12	Tower Wind monitor	Young, model 5103L	1 to 50 m s^{-1}, 360˚	±0.3 m s^{-1}, ±5°
13	Ultrasonic anemometer	Young, model 81000	0 to 40 m s^{-1}, 360˚	±3 %, ±5°
15	Wall Pyranometer	Eppley PSP	0.285 to 2.8 µm	±3 %
16	Infrared Radiometer	Eppley PIR	4 to 50 µm	±5 Wm^{-2}
17	Nozzle inlet Temp.	Type T, thermocouple	-25 to 50˚C	±0.5 K
18	Horizontal Pyranometer	Delta T SPN1-A3925	0.4 to 2.7 µm	±8 %
19	Temperature/humidity	Vaisala HMP155	-80 to 60ºC 0 to 100% RH	±1 %
20	Ambient temperature	Type T, thermocouple	-25 to 50˚C	±0.5 K

Note*: accuracy stated for typical operating conditions.

3. Results

3.1 Analyses of Results

Tests were performed from the 18th of December 2023 to the 24th of March 2024. Part way through the test period, the flowrate through the collector was adjusted to investigate the effects of array flow rate and suction velocity through the absorber surface. For this current study, specific clear days from the complete monitoring dataset were selected for detailed study. Each of the days selected was analyzed to determine the instantaneous power output over the course of daylong periods and to determine the total energy delivered during the day. Values of instantaneous and average daily efficiency were calculated. To determine the solar collector net power output, $\dot{Q}_{col}$ was calculated accounting for positive or negative heat gain through the back wall of the building, i.e.,

$$\dot{Q}_{col} = \left(\dot{m} \cdot Cp_m \cdot \Delta T \right) - \dot{Q}_{wall}, \text{ (W)} \qquad \text{(eq. 1)}$$

where $\dot{m}$ is the air mass flowrate (kg s^{-1}),

Cp_m = Specific heat capacity of moist air (kJ $kg^{-1}K^{-1}$)

$$\Delta T = T_{out} - T_a, \text{ (K)} \qquad \text{(eq. 2)}$$

where T_{out} is the temperature of the air exiting the collector (ºC), and

T_a is the temperature of the ambient air entering the collector (ºC).

$\dot{Q}_{wall}$ is the rate of heat transmission through the building wall into the solar collector air channel due to building heat loss.

$$\dot{Q}_{wall} = U_{wall} \cdot A_{col} \cdot \left(T_{building} - T_{eff} \right), \text{ (W)} \qquad \text{(eq. 3)}$$

U_{wall} is the thermal conductance of the wall (0.6 W m^{-2} K^{-1}, (Coenen, 2016), A_{col} is the collector surface area (97.9 m^2), and $(T_{building} - T_{eff})$ is the temperature difference between the building interior and the effective air

temperature in the solar collector air channel (K). Daily values of collected energy were calculated by numerically integrating the measured data over the course of daylong periods, i.e.,

$$Q_{day} = \frac{1}{1000} \cdot \int_{sunrise}^{sunset} \dot{Q}_{col}\, dt \qquad \text{(eq. 4)}$$

where Q_{day} is the total solar energy delivered to the building over a daylong period in kJ or expressed in kWh as $Q_{day,kWh} = Q_{day}/ 3600$.

It is important to determine the collector array's thermal efficiency to allow product comparisons and design improvements. The instantaneous efficiency (expressed as a percentage) for the solar collector was calculated as:

$$\eta_{wall} = 100 \cdot \frac{\dot{Q}_{col}}{(G_i + Ms) * A_{col}} \qquad \text{(eq. 5)}$$

where G_i = Total incident solar radiation on the surface of the collector (W m^{-2}), and

Ms = Net radiant emissive power from the surface of the solar wall (W m^{-2}).

It is worth noting that the calculated value of Ms was effectively zero due to the fact that the solar collector's emittance was very low (0.025) and the surroundings adjacent to the installation were usually snow covered during the monitoring period.

The daily efficiency for the solar collector wall was calculated as a percentage, i.e.,

$$\eta_{daily} = 100 \cdot \frac{Q_{day}}{(H_i/1000) * A_{col}} \qquad \text{(eq. 6)}$$

where H_i is the total irradiance striking surface of the solar collector absorber over the course of a day in J m-2.

3.2 Experimental Results

For this current study, specific days were chosen for detailed analysis, representative of the solar collector's performance at two system flow rates. Typical results for one of the days (March 23rd, 2024) are shown below in Figures 8 to 11. The flow rate through the solar collector was a nominal 2.65 ±0.05 kg s^{-1} and the wind speed was 0.9±0.3 m s^{-1} on that day. Figure 9 shows the variation of collector efficiency over the day. The plot shows unrealistic solar efficiencies in the early morning, most likely due to heat transmission through the building wall when the solar radiation was very low. The rise in effective efficiency later in the day is most likely due to the release of stored heat in the collector and building wall. The plots shown for the 23rd show the effects of the collector's orientation directed to the east of south (53^{o} SE), Fig. 10. This explains why solar irradiance on the wall is skewed toward the morning hours, while the global horizontal irradiance is centered around "solar" noon. Solar irradiance on the wall suddenly drops to a low value as the sun moved behind the building's wall.

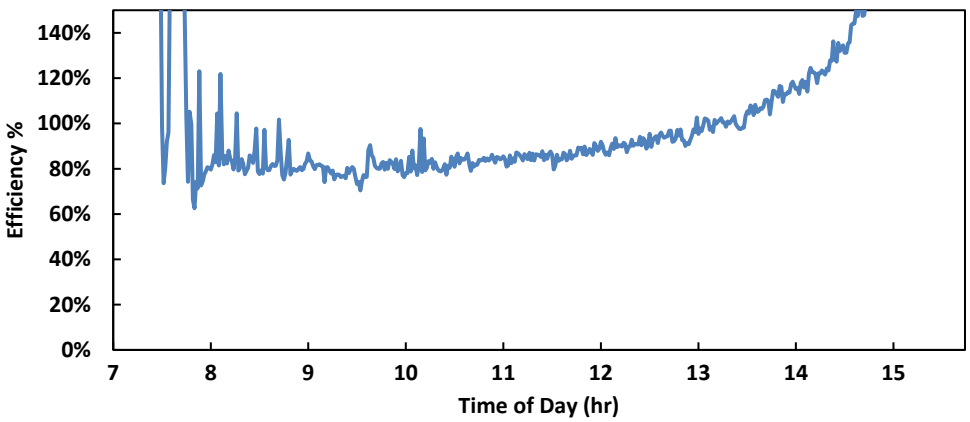

Fig. 9: Apparent Solar collector Efficiency as measured over March 23, 2024.

Figures 11 shows the daily variation of collector inlet and outlet temperatures, and Figure 12 shows the corresponding power output of the collector and cumulative energy.

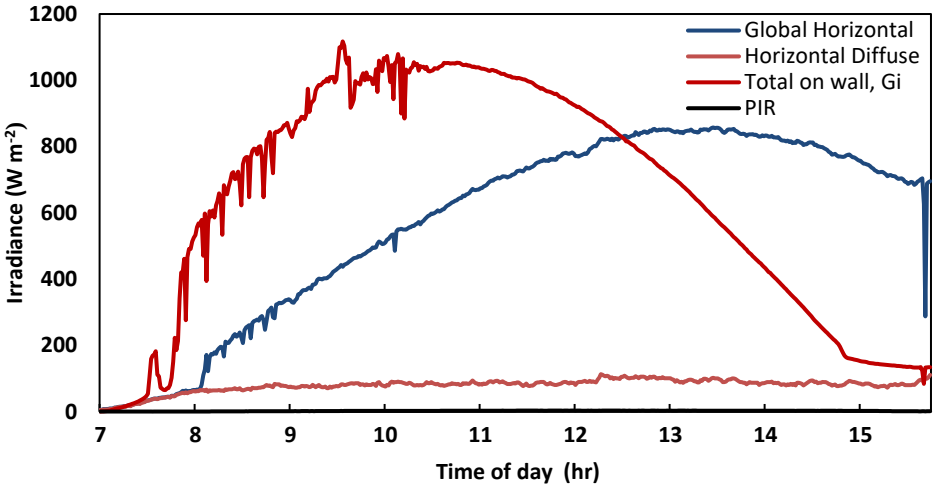

Fig. 10: Solar Irradiance measured over the course of March 23rd, 2024

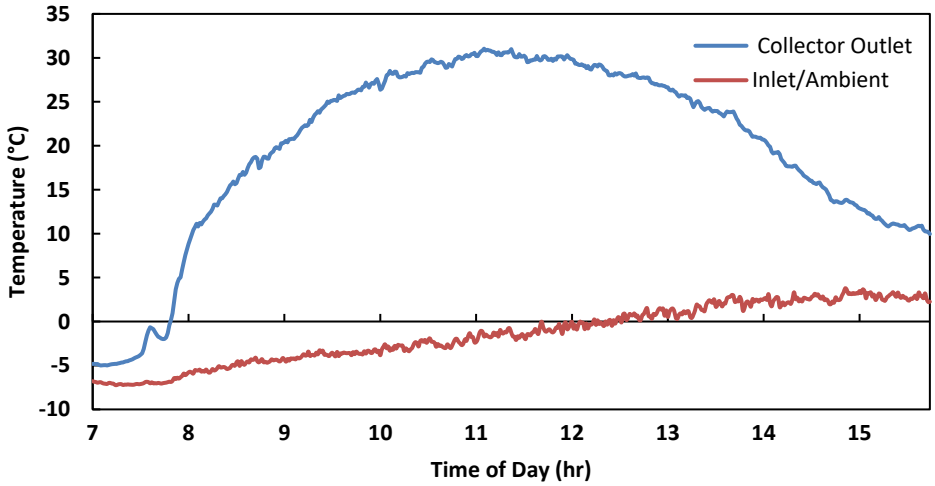

Fig. 11: Inlet and outlet temperatures for the solar collector as measured over the course of March 23rd, 2024. The ambient air temperature in front of the solar collector is taken as the inlet temperature.

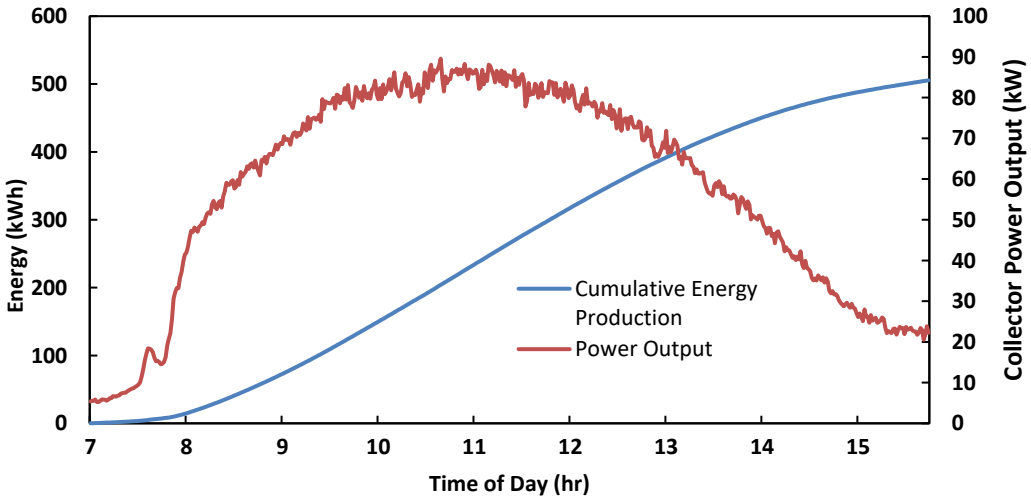

Fig. 12: Cumulative energy and power measured over the course of March 23rd, 2024

A good indication of instantaneous collector efficiency may be obtained by taking the values when the solar collector is operating in a more steady-state condition centered around the peak irradiance time period, e.g., between 10:00 and 11:00 am. Considering this region shown in Figure 9, the collector efficiency is seen to be above 80%. This high value is indicative of the low convective loss as ambient air is drawn through the collector and the Low-e absorber coating that reduces thermal radiation exchange with the surrounding environment. As the temperature of the solar collector increased over the day, the rate of heat transmission through the wall was reduced to insignificant values.

3.2.1 Daily Energy Delivered and Daily Collector Efficiency for Selected Days

To further illustrate the performance of the collector array, total energy delivered over the course of the day was calculated for 5 days with high solar irradiance (i.e., clear days). The daily solar energy delivered to the building and average daily efficiency for the 5 days is given in Table 3 and plotted in Figures 13 and 14.

Tab. 3: Summary of energy production and efficiency for clear days

High Solar Days	Average Daily Ambient Air Temperature (°C)	Average solar Irradiance on solar collector (W m^{-2})	Array Energy Production over Day (kWh)	Average Daily Efficiency	Average Flow Rate Kg s^{-1} m^{-2}
23-Mar	-0.5	487	551	82%	2.70
24-Mar	-2.5	584	454	85%	2.75
13-Mar	16	383	413	83%	2.50
15-Jan	-10	471	270	70%	2.44
26-Feb	5.8	596	328	81%	3.83
11-Mar	4.20	544	317	70%	2.33

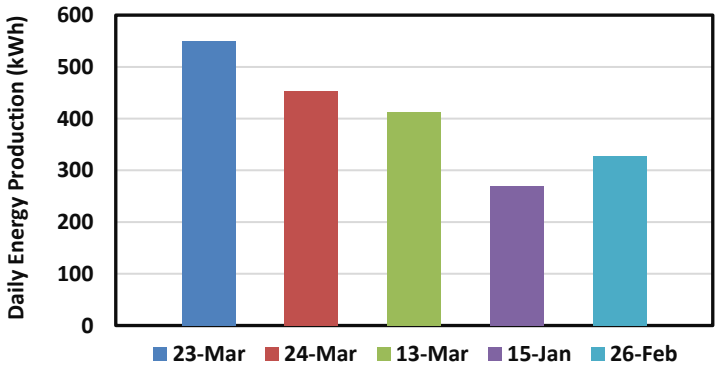

Fig. 13: Summary of energy production for selected clear days

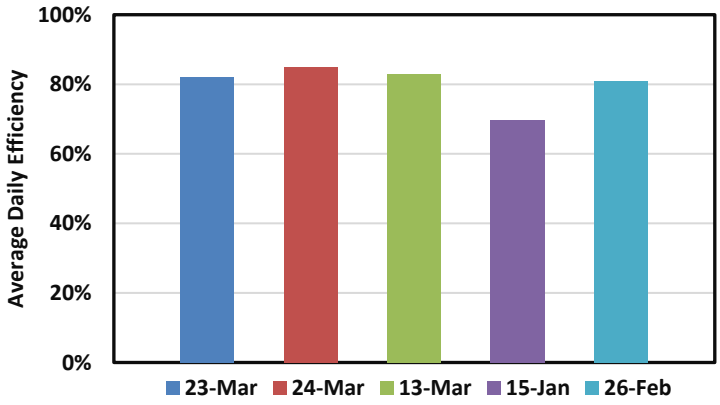

Fig. 14: Summary of collector efficiency for selected clear days

4. Discussion of Results

From the limited results shown if this paper, it is evident that transpired solar air systems operate at high efficiency when drawing ambient air. This is particularly advantageous if industrial or institutional applications require large quantities of fresh air. Currently there are no widely accepted test protocols to evaluate large-scale transpired solar collectors. In their absence, small scale samples have been tested under standard laboratory conditions allowing products to be listed for sale in certain jurisdictions.

In the case considered, a scaled version of the transpired solar collector with low emittance absorber was previously tested under laboratory conditions (SRCC, 2020, Fraunhofer, 2020) in a solar simulator facility. Tests were conducted under steady-state conditions according to the general requirements of ISO 9806. Consequently, these test conditions imposed during this standard test sequence, differed from those experienced in the field installation, including the ambient and inlet temperatures, solar irradiance intensity, and wind direction and velocity and characteristics (e.g., turbulence). A summary of the major differences between the standard test sequence and the test conditions experienced during this field trial are given below in Table 4.

Tab. 4: Comparison of test ISO- 9806 test conditions with large-scale tests

ITEM	ISO 9806 Standard Laboratory Test Sequence	NSTF large-Scale collector
Angle of tilt	45 ˚ to horizontal	Vertical
Infrared losses/gains	Higher effective sky temp due to simulator lamps and surroundings temperatures	Colder effective sky and surroundings temperatures
Wind direction	Scroll up from bottom of collector	Random, Turbulent
Ratio of Aperture to Gross collector area	Aperture = 2.43, Gross= 2.56 m^2 (Ratio = 0.95)	Negligible
Area of panel	Small, 2.56 m^2	Large, 98 m^2
Ambient air temperature	298 K (25ºC)	253 to 293 K (-20 to 20ºC)

The monitored test data obtained at the National Solar Test Facility show that the flow conditions adjacent to the large solar collector array were highly complex, with the various components of the air flow velocity varying rapidly in time, consistent with a turbulent flow condition. An example plot of air flow direction and velocity is shown in Figure 15, as measured using the three-axis ultrasonic wind transducer located at approximately 2.5 meters from the solar collector surface. The effects of turbulence intensity on unglazed transpired solar air collectors have been investigated in earlier studies (Fleck et al., 2002) and will be the focus future studies based on the data measured on the large collector array at the NSTF. The full wind data set was recorded at high frequency (4 times per second) to capture the rapid changes in velocity. It is also expected that the effects of wind on solar collector performance will depend on the air flow velocity through the solar collector as higher suction velocities at the surface may also affect boundary layer development and heat loss from the collector surface.

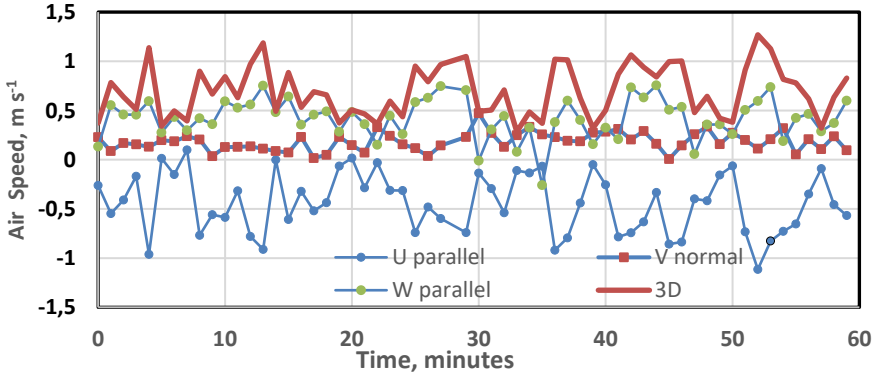

Fig. 15: Plot of 1-minute averages of the vector components of wind speed, as measured with the 3-axis ultrasonic wind transducer located in front of the collector surface, shown for a one hour-long period, i.e., 12 to 1 pm on January 15th, 2024. The vector sum is also shown, labeled 3D, and calculated as the root-mean square of the three velocity vectors. This plot illustrates the variability of the wind direction and velocity adjacent to the test wall.

4.1 Comparison with Previous Test Data

As an initial comparison, the NSTF monitored data was compared with standard laboratory results published by SRCC (SRCC, 2020) and based on tests conducted on a scaled collector sample according to the general requirements of the ISO 9806 (ISO 9806, 2017) test procedure. To facilitate this comparison, NSTF outdoor data was selected from "high irradiance" and "quasi-steady-state" periods at near-normal incidence angles. As ambient air temperatures were not the same, the data was compared to a performance characteristic derived from the laboratory test results and plotted as a function of the temperature difference between ambient inlet air temperature, Ta, and the average of the collector inlet and outlet air temperatures, Tm.

The results of this comparison are show in Figure 16, where the solid line indicates the approximate performance characteristic derived from the laboratory testing of the scaled sample (SRCC, 2020). The data points shown on the graph were derived from the NSTF monitored data taken on the large-scale solar collector. It may be seen that at higher flow rates and lower values of (Tm-Ta) the results correspond well. However, at higher values of (Tm-Ta) the output per unit area for the large-scale collector are higher than the laboratory derived result. These results suggest that the airflow associated with wind velocity around the large-scale collector differ from those experienced during laboratory testing. As well, the large-scale collector would have lower edge effects including heat losses, when compared to the small sample. One would expect that at higher collector flowrates through the perforated absorber plate, heat transfer would be greater, but the overall temperature rise, and resultant Tm would be lower. This would increase overall efficiency but at the cost of a lower delivery temperature to the building.

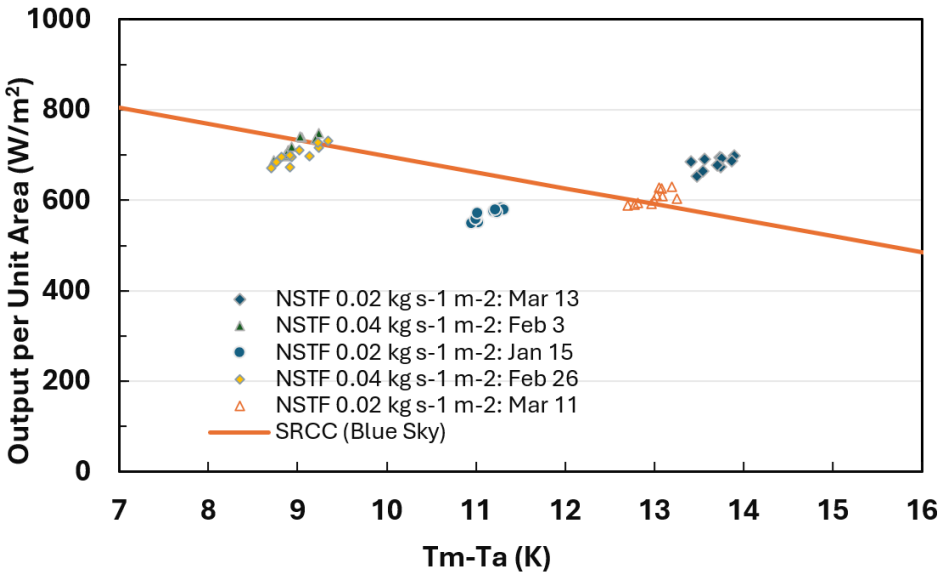

Fig. 16: Comparison of data selected from the large collector test at the NSTF with a performance characteristic derived from standard test results conducted on scaled samples (SRCC, 2020).

5. Conclusions

An extensive data set on the performance of a large scale transpired air solar collector has been collected under real atmospheric conditions. High level monitoring and data acquisition was used to record both the atmospheric and thermal performance data. The preliminary results have shown that the transpired collector with low emittance absorber coating can achieve high thermal efficiency while delivering solar preheated air.

The preliminary results indicate that differences in predicted performance exist between the large-scale installations and tests conducted on scaled samples and these increase at higher values of (Tm-Ta).

While this project has obtained significant data on the performance of transpired solar collectors, additional analysis is required to fully quantify the effects of the various variables. The results also indicate that the development of an appropriate test standard for transpired solar air collectors should be undertaken. With this in mind, a future endeavour will focus characterizing the performance of the large-scale transpired collector installation through regression analysis conducted on the monitored data, similar to that proposed for outdoor dynamic testing liquid-based solar collectors in ISO 9806.

6. Acknowledgments

The authors gratefully acknowledge the financial support of Natural Resources Canada through the Office of Energy Research and Development – Energy Innovation Program (EIP).

7. References

Brunger, A.P., Cali, A., Kutscher, C.F., Dymond, C.S., Pfluger, R., McClenahan, D., Kokko, J. and Hollick, J., 1999. Low cost, high performance solar air-heating systems using perforated absorbers. IEA International Energy Agency Solar Heating and Cooling Task 14 report – Air Systems Working Group.

Coenen, M., Exova Canada Inc., NRCan Report, 2016. Evaluation of Foam Insulation from the NSTF Lab Wall for Thermal Properties in Accordance with ASTM C518-15.

Fleck, B.A., Meier, R.M. and Matović, M.D., 2002. A field study of the wind effects on the performance of an unglazed transpired solar collector. Solar energy, 73(3), pp.209-216.

Fraunhofer-Institut für Solare Energiesysteme ISE, 2020. Test report according to EN 12975-1:2006+A1:2010 /EN ISO 9806:2017, Report KTB: 2020-02-k2.

ISO 9806:2017, 2017. International Standards Organization. Solar energy – Solar thermal collectors – Test Methods. https://www.iso.org/standard/67978.html, accessed August 1, 2024.

Kutscher, C.F., Christensen, C. and Barker, G., 1991. Unglazed transpired solar collectors: an analytic model and test results. In Proceedings of ISES Solar World Congress (Vol. 2, pp. 1245-1250).

Shukla, A., Nkwetta, D.N., Cho, Y.J., Stevenson, V. and Jones, P., 2012. A state of art review on the performance of transpired solar collector. Renewable and Sustainable Energy Reviews, 16(6), pp.3975-3985.

SRCC, Solar Rating and Certification Corporation. 2020. Report OG-100 ICC-SRCC Certified Solar Air Heating Collector #10002111. https://solar-rating.org/, accessed August 1, 2024.